Chemical Science

ROYAL SOCIETY OF CHEMISTRY

EDGE ARTICLE

View Article Online
View Journal | View Issue

Cite this: *Chem. Sci.*, 2025, **16**, 20931

All publication charges for this article have been paid for by the Royal Society of Chemistry

Unusual "mesoionic" N^S biscyclometallated iridium(III) polypyridine complexes as photosensitisers for photodynamic therapy and type II immunogenic cell death inducers

Justin Shum, [ab] Peter Kam-Keung Leung, [ac] Lili Huang, [a] Lawrence Cho-Cheung Lee, [ab] Maryana Yarshova, [a] Lin Cheng, [a] Yi Pan, [a] Michael Wai-Lun Chiang, [a] Ken Shek-Man Yiu,[a] Kai-Chung Lau, [a] Ben Zhong Tang [de] and Kenneth Kam-Wing Lo *[ac]

Received 28th June 2025
Accepted 12th September 2025

DOI: 10.1039/d5sc04772b

rsc.li/chemical-science

Historically, the classification of mesoionic compounds has been disconcerting, with more confusion arising when these molecules are used as ligands for metal complexes. Many mesoionic compounds are also biologically active and widely used in various therapeutic applications, but mesoionic metal complexes have not seen much prevalence in the field. In this work, we determine the "mesoionic" nature of an unusual and rare series of N^S biscyclometallated iridium(III) complexes $[Ir(N^C)_2(p\text{-}ttqt)]$ (p-Httqt = 1-phenyl-5-thioxo-5,6-dihydro-[1,2,4]triazolo[1,5-*c*]quinazolin-1-ium-2-thiolate; HN^C = 2-phenylpyridine (Hppy) (**1**), 7,8-benzoquinoline (Hbzq) (**2**), 2-phenylbenzothiazole (Hbt) (**3**) and 2-(1-naphthyl)benzothiazole (Hbsn) (**4**)) as photodynamic therapy (PDT) agents and immunogenic cell death (ICD) inducers. X-ray, infrared spectroscopy and density functional theory studies demonstrate that the mesoionic nature is retained in the iridium(III) complexes. These complexes are ideal PDT agents with no cytotoxicity at micromolar concentrations ($IC_{50,dark}$ > 25 μM), remarkable photocytotoxicity at nanomolar concentrations and PI values ($IC_{50,light}$ = 1.5–69 nM; PI = 362–33 333), and exquisite selectivity towards cancer cells. Furthermore, their localisation in the endoplasmic reticulum (ER) and efficient reactive oxygen species (ROS) generation enable them to act as photoactivated type II ICD inducers.

Introduction

Mesoionic compounds are structurally defined as five-membered heterocyclic rings that cannot be satisfactorily represented by any single resonance structure and possess a dipolar nature with a localised positively charged ring counterbalanced by a negatively charged exocyclic atom (Scheme 1).[1] The term "mesoionic" has been highly debated, with the most recent calculations highlighting the absence of aromaticity and the exocyclic bond showing more of a double bond character.[2,3] As an extension, a class of compounds rarely investigated is transition metal complexes with intact mesoionic character. However, these complexes heavily rely on mesoionic sydnone as the coordinating ligand, and most work only reports their synthesis.[4] The rarity of mesoionic transition metal complexes and the lack of variation in mesoionic ligands is attributable to their difficult and poorly understood preparation and purification procedures, instability, ambiguous chelation modes to the metal centre, and the mesoionic properties that are uncertain after coordination. In a therapeutic context, mesoionic compounds are highly bioactive and have been investigated for anti-bacterial, anti-cancer and anti-inflammatory applications.[5–10] This popularity has not extended to

[a]*Department of Chemistry, City University of Hong Kong, Tat Chee Avenue, Kowloon, Hong Kong, P. R. China. E-mail: bhkenlo@cityu.edu.hk*

[b]*Laboratory for Synthetic Chemistry and Chemical Biology Limited, Units 1503-1511, 15/F, Building 17 W, Hong Kong Science Park, New Territories, Hong Kong, P. R. China*

[c]*State Key Laboratory of Terahertz and Millimetre Waves, City University of Hong Kong, Tat Chee Avenue, Kowloon, Hong Kong, P. R. China*

[d]*Department of Chemistry, The Hong Kong University of Science and Technology, Clear Water Bay, Kowloon, Hong Kong, P. R. China*

[e]*School of Science and Engineering, Shenzhen Institute of Aggregate Science and Technology, The Chinese University of Hong Kong, Shenzhen (CUHK-Shenzhen), Shenzhen, Guangdong, 518172, P. R. China*

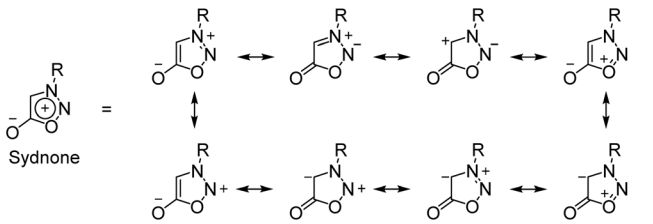

Scheme 1 Resonance structures of sydnone, a representative mesoionic compound.

mesoionic transition metal complexes due to the aforementioned issues, but research in this frontier area is necessary to elucidate their biological activity and develop new diagnostic and therapeutic tools.

Recently, the synthesis of a new class of fused mesoionic compounds, 1-substituted-5-thioxo-5,6-dihydro-[1,2,4]triazolo-[1,5-*c*]quinazolin-1-ium-2-thiolate (Httqt),[11] inspired us to attempt the coordination with an iridium(III) metal centre. Cyclometallated iridium(III) complexes enable facile attachment of ligands in mild reaction conditions (stirring at room temperature), which is crucial since harsher conditions may affect the stability of the mesoionic ligand. Additionally, cyclometallated iridium(III) complexes are potent photosensitisers for photodynamic therapy (PDT) due to their high biocompatibility, luminescence and ability to generate reactive oxygen species (ROS).[12–19] Furthermore, luminescent iridium(III) complexes have been shown to be effective immunogenic cell death (ICD) inducers.[20–23] The demand for PDT agents that can activate type II ICD response is increasing since these compounds are expected to directly induce endoplasmic reticulum (ER) stress and promote anti-tumour immunity in a controlled manner.[24–26]

Herein, we report the synthesis, characterisation and photophysical and photochemical properties of an unusual and rare class of neutral mesoionic N^S biscyclometallated iridium(III) complexes [Ir(N^C)$_2$(p-ttqt)] (p-Httqt = 1-phenyl-5-thioxo-5,6-dihydro-[1,2,4]triazolo[1,5-*c*]quinazolin-1-ium-2-thiolate; HN^C = 2-phenylpyridine (Hppy) (**1**), 7,8-benzoquinoline (Hbzq) (**2**), 2-phenylbenzothiazole (Hbt) (**3**) and 2-(1-naphthyl) benzothiazole (Hbsn) (**4**)) (Scheme 2), and their use as potent photosensitisers and type II ICD inducers. The structures and "mesoionic" nature of the iridium(III) complexes **1**, **2** and **4** were characterised by X-ray crystallography and density functional theory (DFT) studies. The photophysical properties, electrochemical behaviour and singlet oxygen ($^1O_2$) generation quantum yields of the complexes, as well as the photoinduced oxidation of 1,4-dihydronicotinamide adenine dinucleotide (NADH) by the complexes were examined. Additionally, the aggregation-induced emission (AIE) properties of the complexes were determined. The cellular uptake and localisation of the complexes were also studied by inductively coupled plasma-mass spectrometry (ICP-MS) and laser-scanning confocal microscopy (LSCM), respectively. The (photo)cytotoxicity of the complexes against cancer and normal cells was evaluated using the 3-(4,5-dimethylthiazol-2-yl)-2,5-diphenyltetrazolium bromide (MTT) assay. Complex **2** was shown to be the most effective photosensitiser and was used to demonstrate the photoinduced activation of the cell death mechanism and ICD response by using various biological markers.

Results and discussion

Synthesis and characterisation

The ligand p-Httqt was synthesised as previously reported.[11] The thiourea intermediate was synthesised by condensation of methyl-2-isothiocyanatobenzoate with 4-phenyl-thiosemicarbazide. Base-catalysed cyclisation of the intermediate thiourea derivative yielded the p-Httqt ligand. The ppy (**1**), bzq (**2**), bt (**3**) and bsn (**4**) complexes were prepared from the reaction of the corresponding iridium(III) dimers [Ir$_2$(N^C)$_4$Cl$_2$] with p-Httqt and Et$_3$N in CH$_2$Cl$_2$/MeOH, purified by column chromatography and recrystallised from CH$_2$Cl$_2$/(CH$_3$)$_2$CO/Et$_2$O. All the complexes were characterised by ^{1}H and ^{13}C NMR spectrometry, high-resolution ESI-MS and IR spectroscopy, and their elemental analyses were satisfactory. X-ray crystal structures of complexes **1**, **2** and **4** were also investigated. Detailed synthetic procedures and characterisation data are included in the SI.

Structure and mesoionic elucidation

Biscyclometallated iridium(III) complexes have been reported to coordinate N^S ligands *via* 3-atom or 4-atom chelation.[27,28] The presence of multiple nitrogen and sulfur atoms on the Httqt ligand could enable facile attachment *via* N^S chelation to the iridium(III) metal centre, but the coordinating modes can occur in three forms (Fig. 1a). During the purification process of the iridium(III) complexes, we noticed that only one single product was formed. Interestingly, ^{1}H NMR analyses of the iridium(III) complexes indicated that after coordination, deprotonation of the amine present on the 1,2,4-triazolo[1,5-*c*]quinazolin-1-ium-2-thiolate ring (Fig. 1b and S1) of the p-Httqt ligand occurred and this phenomenon is evidenced by the missing broad peak at δ 14.47 in all the complexes (Fig. 1b and S2–S5). To elucidate the structural form, single crystals of complexes **1**, **2** and **4** were

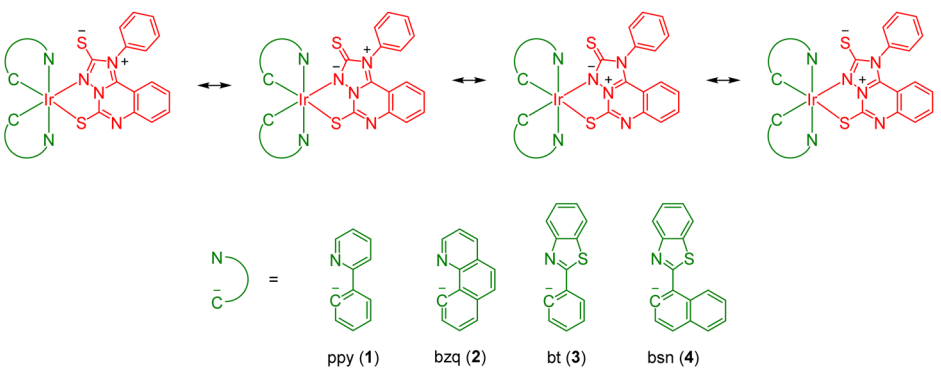

Scheme 2 Resonance structures of the mesoionic N^S iridium(III) complexes **1**–**4**.

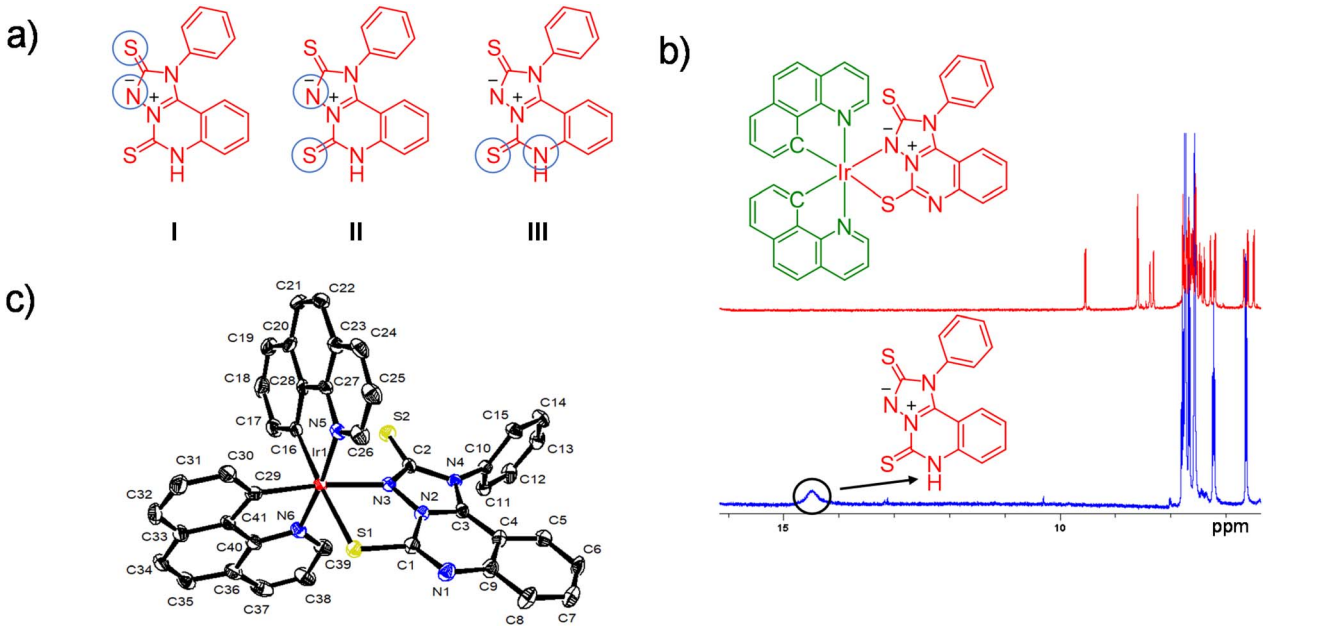

Fig. 1 (a) Different coordination modes I–III of p-Httqt for N^S chelation. (b) Magnified ^{1}H NMR spectra of complex **2** (red) and p-Httqt ligand (blue) in DMSO-d_6. (c) Perspective drawing of complex **2** with the atomic labelling scheme. Thermal ellipsoids are shown at the 35% probability level. Hydrogen atoms are omitted for clarity.

obtained by slow diffusion of Et_2O vapour into a concentrated $CH_2Cl_2/(CH_3)_2CO$ solution of the respective complex. Crystal and structure determination data of the complexes are listed in Tables S1–S3. Selected bond lengths and angles of complexes **1**, **2** and **4** are listed in Tables S4–S6, respectively. The perspective drawings of complexes **1**, **2** and **4** are depicted in Fig. S6, 1c and S7, respectively. The structures obtained from X-ray crystallography data demonstrate that the N^S iridium(III) complexes preferentially adopt coordination form II (Fig. 1a). The iridium(III) centre of **1**, **2** and **4** adopts a distorted octahedral geometry, and the *trans* angles at the metal centre range from 170.4 to 178.4°, 173.0 to 175.2° and 169.4 to 175.5°, respectively. The Ir–C bonds of the cyclometallated ligands are coordinated to the iridium(III) centre in a *cis* configuration. The *trans*-influence of the carbon donors results in a longer Ir–N bond length in the p-ttqt ligand for complexes **1** (Ir(1)–N(3), 2.171 Å), **2** (Ir(1)–N(3), 2.144 Å) and **4** (Ir(1)–N(3), 2.181 Å) than in their cyclometallating ligands (ppy = Ir(1)–N(5), 2.040 Å; Ir(1)–N(6), 2.070 Å, bzq = Ir(1)–N(5), 2.072 Å; Ir(1)–N(6), 2.042 Å and bsn = Ir(1)–N(5), 2.070 Å; Ir(1)–N(6), 2.056 Å). The bite angles of the cyclometallating ligands (N–Ir–C) and the p-ttqt ligand (N–Ir–S) are close to 80°; similar observations have been made in a related N^S biscyclometallated iridium(III) polypyridine system.[27,29] The phenyl ring and the 1,2,4-triazole ring of the p-ttqt ligand for **1**, **2** and **4** are non-conjugated, and the dihedral angles were determined to be 87.90, 83.97 and 68.60°, respectively, suggestive of a lack of π-conjugation.

In accordance with other reported mesoionic systems,[2,32] we determined if the iridium(III) complexes are mesoionic based on two factors: (1) double bond character in the exocyclic bond and (2) the absence of aromaticity in the 5-membered ring. In complexes **1**, **2** and **4**, the p-ttqt C(2)–S(2) bond lengths are 1.660, 1.647 and 1.650 Å, respectively. These bond length values are noticeably shorter than the average value for compounds with C–S single bonds (1.804 Å),[33] and slightly longer than C=S double bonds (1.602–1.628 Å).[34–36] These data suggest that the bonding in these complexes is a combination of resonance structures that feature substantial C=S double bond character. IR spectroscopy measurements also confirmed the presence of an absorption peak ascribed to a C=S double bond (*ca.* 1320 cm^{-1}). A similar observation has been made in a structurally related compound.[33] The C–N bond lengths of the 1,2,4-triazole ring in complexes **1**, **2** and **4** are in the range of 1.332–1.430 Å with a significantly longer C(2)–N(4) bond (complex **1** = 1.421 Å, complex **2** = 1.415 Å and complex **4** = 1.430 Å). The variation in bond lengths connecting the same atom types (C–N) indicates that the geometric standards for aromaticity are not respected; this agrees with recent calculations of mesoionic azomethine ylides and imines.[2] Based on the criteria for mesoionic compounds,[30–32,37] the combined X-ray and IR spectroscopy results showing the double bond character of the C(2)–S(2) and lack of aromaticity in the p-ttqt ligand are suggestive of retention of the mesoionic character of the ligand upon coordination to the iridium(III) centre.

To further elucidate the electronic structure and mesoionic nature of the complexes, DFT calculations were performed at the B3LYP-D3(BJ)/def2-SVP and B3LYP-D3(BJ)/def2-TZVP levels using **1** as the model complex. Geometry optimisation studies of the ground state (S_0) were carried out using the polarisable continuum model (PCM) to account for solvation effects in CH_2Cl_2. The optimised bond lengths and bond angles of the S_0 structure (Table S7) show excellent agreement with the X-ray crystallographic data, with mean absolute deviations (MADs) of 0.013–0.019 Å for selected bond lengths and 1.37–2.14° for

bond angles. The calculated Wiberg bond indices (Fig. S8) support the absence of aromatic character in the five-membered ring. Specifically, the bond orders are S(2)–C(2), 1.51; N(4)–C(2), 0.99; N(4)–C(3), 1.20; N(2)–C(3), 1.19; N(2)–N(3), 1.07; and N(3)–C(2), 1.30. These values indicate that S(2)–C(2) and N(3)–C(2) bonds possess partial double character, whereas N(4)–C(2) and N(2)–N(3) are essentially single bonds.

Photophysical and photochemical properties

The electronic absorption spectral data of the p-Httqt ligand and the complexes are listed in Table S8, and the electronic absorption spectra of the ligand and the complexes are shown in Fig. 2a and S9. All the complexes displayed intense spin-allowed intraligand (^{1}IL) ($\pi \rightarrow \pi^*$) (N^S and N^C) absorption features in the UV region (*ca.* 250–349 nm, ε on the order of 10^4 dm^3 mol^{-1} cm^{-1}) and weaker spin-allowed metal-to-ligand charge-transfer (^{1}MLCT) (dπ(Ir) $\rightarrow$ π^*(N^S and N^C)) transitions (*ca.* 350–450 nm). The weaker absorption tailing beyond *ca.* 475 nm is assigned to spin-forbidden ^{3}MLCT (dπ(Ir) $\rightarrow$ π^*(N^S and N^C)) transitions for complexes **1–3**. The spin-forbidden ^{3}MLCT (dπ(Ir) $\rightarrow$ π^*(N^S and N^C)) transitions for complex **4** are attributed to the weaker absorption tailing beyond *ca.* 490 nm. The assignment of these bands is made with reference to previous spectroscopic studies of bi-cyclometallated iridium(III) complexes.[27,38–42] Upon photoexcitation, the complexes exhibited moderately intense and long-lived greenish-yellow to red emission in solutions under ambient conditions and in low-temperature glass. The photophysical data of the ligand and complexes are shown in Table S9, and the emission spectra of the ligand and complexes are presented in Fig. 2b and S10. The ppy (**1**) and bzq (**2**) complexes showed a broad and featureless emission band in fluid

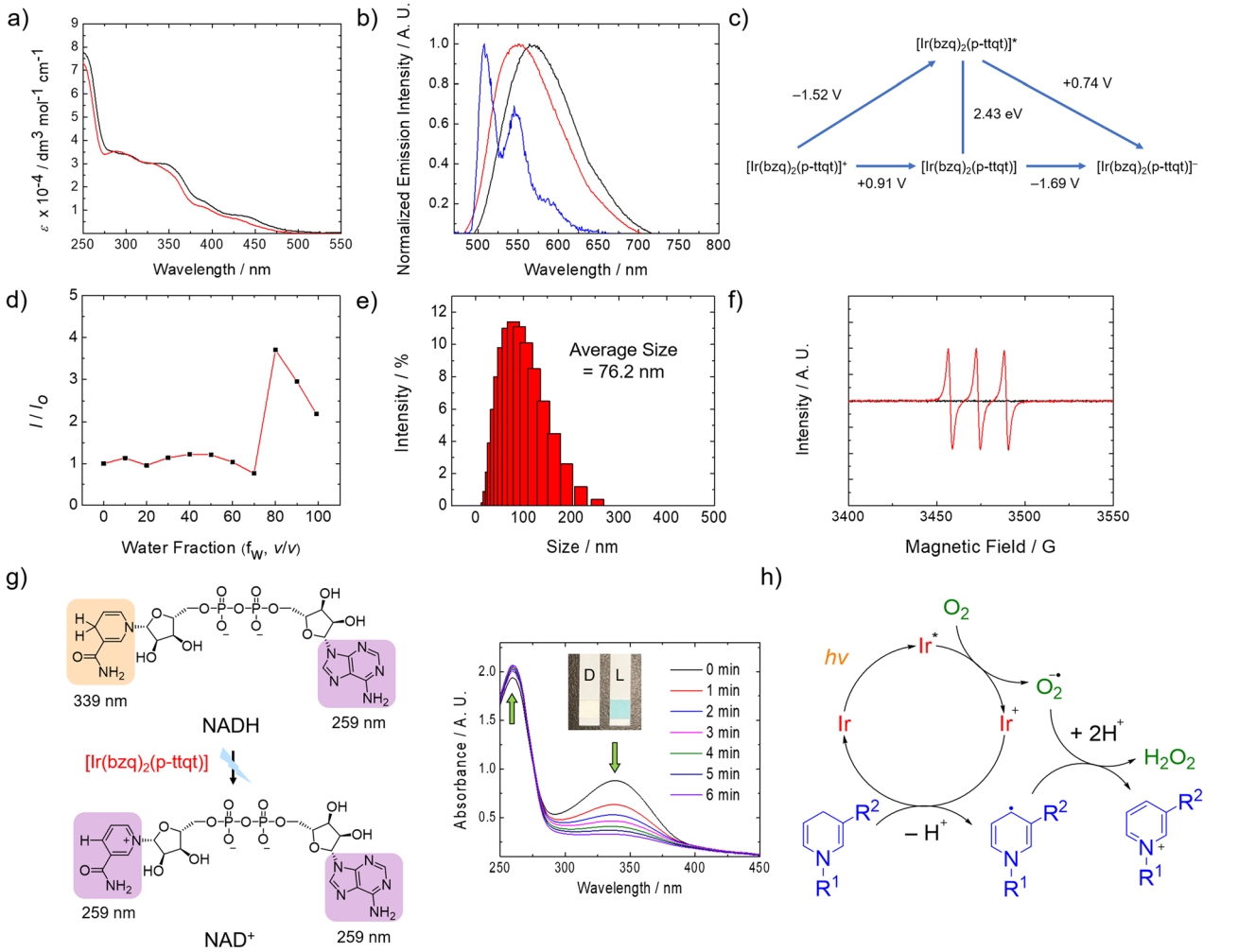

Fig. 2 (a) Electronic absorption spectra of complex **2** in CH_2Cl_2 (black) and CH_3CN (red) at 298 K. (b) Normalised emission spectra of complex **2** in CH_2Cl_2 (black) and CH_3CN (red) at 298 K and in *n*-butyronitrile at 77 K (blue) (λ_{ex} = 350 nm). (c) Latimer diagram showing the ground- and excited-state potentials of complex **2** in CH_3CN at 298 K; potentials are with reference to the SCE. (d) Relative emission intensities of complex **2** (10 μM) in aerated CH_3CN solutions with various water fractions (f_w, v/v) at 298 K (λ_{ex} = 350 nm). (e) Size distribution of complex **2** (10 μM) in water/DMSO (99 : 1, v/v). (f) ESR signals obtained without (black) and with (red) irradiation at 450 nm (15.5 mW cm^{-2}, 15 min) of aerated CH_3CN solutions containing TEMP (20 mM, $^1O_2$ scavenger) and complex **2** (10 μM). (g) Photooxidation of NADH (100 μM) with complex **2** (10 μM) upon light irradiation (450 nm, 15.5 mW cm^{-2}) at different time intervals in water/DMSO (99 : 1, v/v). Inset: detection of H_2O_2 after irradiation (D = dark; L = light). (h) Proposed photocatalytic cycle for the oxidation of NADH by complexes **1–4**.

solutions at 298 K, indicative of a ^{3}MLCT (dπ(Ir) → π^*(N^S))/^{3}ligand-to-ligand charge-transfer (LLCT) (π(N^C) → π^*(N^S)) emissive state.[27,38–42] However, complexes **3** and **4** displayed a structured band suggestive of a ^{3}IL (π → π^*)(N^C) emissive state, probably mixed with some ^{3}MLCT (dπ(Ir) → π^*(N^C/N^S)) character. The emission bands of the complexes showed enriched structural features upon cooling the samples to 77 K, attributed to the increased involvement of ^{3}IL (π → π^*) (N^S and N^C) excited-state character. In general, the emission quantum yields ($\Phi_{em} \geq 0.06$) and emission lifetimes ($\tau_0 \geq 0.24$ μs) of all the complexes are larger than those of previously reported N^S biscyclometallated iridium(III) complexes [Ir(N^C)$_2$(N^S)].[27]

Time-dependent DFT (TD-DFT) calculations for complex **1** were subsequently performed to investigate the nature of the low-lying singlet (S_1–S_3) and triplet (T_1–T_4) excited states. The vertical excitation energies of T_1 (2.51 eV) and T_2 (2.55 eV) are nearly degenerate, while T_3 (2.68 eV) and T_4 (2.72 eV) lie at higher energies (Table S10). Inter-fragment charge-transfer (IFCT) analysis (Table S10) was employed to quantify the contributions of MLCT, LMCT, LLCT, IL and metal-centred character in these excitations. The S_0 → T_1 and S_0 → T_2 transitions are primarily ^{3}IL (π(N^S) → π^*(N^S)), contributing 84.7% and 76.0%, respectively. These are followed by ^{3}MLCT contributions (dπ(Ir) → π^*(N^S)), 9.1% and 15.3% and, to a lesser extent, ^{3}LLCT (π(ppy) → π^*(N^S)), 4.1% and 7.0%, respectively. Natural transition orbital (NTO) analysis of the S_0 → T_1 and S_0 → T_2 excitations also reveals that both the occupied and virtual NTOs are predominantly localised on the N^S ligand (Fig. S11).

The electrochemical properties of the p-Httqt ligand and complexes **1–4** were investigated by cyclic voltammetry, and their electrochemical data are listed in Table S12. Latimer diagrams were constructed based on their electrochemical data, and the excited-state energy of the complexes was calculated from their emission maxima in low-temperature glass. As indicated in Fig. 2c and S12, the excited-state reduction potential ($E^\circ[Ir^{+/*}]$) ranged from −1.06 to −1.52 V *versus* the saturated calomel electrode (SCE), which is more negative than those of typical ruthenium(II) and iridium(III) complexes,[43] highlighting that the complexes are strong photoreductants.

The environment-responsive photophysical properties and $^1O_2$ generation capabilities of the complexes are important for developing robust PDT agents. Thus, the complexes were first investigated for their environment-sensitive emission in aerated CH_3CN solutions with various water fractions (f_w, v/v) at 298 K, and their emission responses are illustrated in Fig. 2d and S13. Complexes **1–3** displayed enhanced emission intensities upon increasing water fractions; however, this enhancement was reduced upon reaching $f_w = 99\%$. The decrease is attributable to the random agglomeration of amorphous aggregates caused by increased solvent polarity and a decrease in the solubility of the complexes.[44,45] The increased emission intensities at various water fractions (f_w = 60–90%) for complexes **1–3** suggest the formation of ordered crystalline nanoaggregates[44,45] and were confirmed by DLS analysis (Fig. 2e, S14 and S15). At $f_w = 99\%$, a composition suitable for biological applications, complexes **1** and **2** showed AIE properties that could be useful in enhancing the emission intensity and photocytotoxicity of the complexes. Complex **4**, possessing the most hydrophobic cyclometallating ligand bsn, however, was AIE-inactive with a decreased emission intensity upon increasing water concentrations, even though the complex also underwent aggregation (Fig. S14 and S15).

The $^1O_2$ quantum yields (Φ_Δ) of the complexes are listed in Table S13, and the Φ_Δ values of the complexes in order of the highest production are **4** > **1** > **2** > **3**. Complex **4** displayed the largest Φ_Δ values which may result from its longest emission lifetime (>2.00 μs, Table S9). To further confirm the $^1O_2$ generation by the complexes, electron spin resonance (ESR) spectroscopy was employed with a $^1O_2$ trapper, 2,2,6,6-tetramethylpiperidine (TEMP). As illustrated in the ESR spectra of the iridium(III) complexes in aerated CH_3CN solutions upon irradiation (Fig. 2f and S16), TEMP is converted to TEMPO after reaction with $^1O_2$, leading to an intense 1 : 1 : 1 triplet signal. This result indicates that all the iridium(III) complexes can photosensitise $^3O_2$ to generate $^1O_2$.

A crucial coenzyme for redox reactions in living cells is NADH, a useful indicator of the cell's metabolic state.[46] Induced conversion of intracellular NADH to NAD^+ in cancer cells can disrupt the redox balance, leading to cell death.[47–51] The characteristic absorption peaks of NADH (λ = 259 and 339 nm) and NAD^+ (λ = 259 nm) were monitored upon treatment with the complexes and light irradiation (Fig. 2g and S17). All the complexes with light irradiation could induce a significant increase and decrease in absorbance at 259 and 339 nm, respectively, indicative of photoinduced conversion of NADH to NAD^+. The complete transformation of NADH was observed within 6 min of irradiation time, and the turnover frequency values of the complexes were determined to be 62.7–69.4 h^{-1} (Table S14). Interestingly, all the complexes showed reduced or no photoinduced conversion of NADH in degassed solutions (Fig. S18), highlighting the role that oxygen plays in the photocatalytic cycle. The high excited-state reduction potentials of the complexes ($E^\circ[Ir^{+/*}] = -1.06$ to −1.52 V *versus* SCE) are more negative than the reduction potential of oxygen to superoxide anions (*ca.* −0.75 V *versus* SCE),[52] indicating that superoxide anions could be formed from oxygen and converted to H_2O_2. Peroxide detection strips (inset of Fig. 2g and S17) confirmed the generation of H_2O_2 and highlighted that the complexes may show similar photocatalytic properties to other previously reported photoreductants.[53,54] A proposed photocatalytic cycle for the oxidation of NADH by complexes **1–4** is shown in Fig. 2h. Notably, the excited-state reduction potentials of the complexes ($E^\circ[Ir^{*/-}]$ = +0.46 to +0.74 V *versus* SCE) is more positive when compared to the reduction potential of $NAD^\bullet + e^- + H^+ \rightarrow$ NADH (*ca.* +0.035 V *versus* SCE),[55] illustrating that the complexes can also feasibly undergo an alternative NADH photooxidation pathway.[56]

Photodynamic therapy efficacy

Based on the promising structural features and chemical properties, the (photo)cytotoxicity of the ligand and complexes

1–4 towards cancer (A549 and HeLa) and normal (MRC9) cells was evaluated using the MTT assay (Table 1). The maximum concentrations tested for the ligand, complexes **1–3** and complex **4** were 100, 50 and 25 μM, respectively, due to solubility reasons. Interestingly, the ligand and complexes were essentially noncytotoxic in cancer and normal cells at their highest soluble concentration (25–100 μM) in the dark for 24 h. This noncytotoxic property could be attributed to the chelation of the noncytotoxic mesoionic N^S ligand; hence, the coordination of p-Httqt to the metal centre could bestow low dark cytotoxicity on the resulting metal complex. Surprisingly, upon photoirradiation, the complexes showed no photocytotoxic activity towards normal cells ($IC_{50,light}$ > 50 μM for complexes **1–3**; $IC_{50,light}$ > 25 μM for complex **4**). This interesting result is further highlighted by the exceptionally large photocytotoxicity index (PI) values obtained for complexes **1–4** (PI = 362–33 333) compared to other luminescent biscyclometallated iridium(III) polypyridine complexes.[57–63]

The cellular localisation of the iridium(III) complexes is important in assessing photoinduced damage since photogenerated ROS have short half-lives and their photocytotoxicity is limited to the surrounding environment. Interestingly, all the complexes showed specific staining of the ER and high Pearson's correlation coefficients ((PCC) = 0.89–0.96, Fig. 3a and S19) with ER-Tracker Red in HeLa cells. This result highlights that the complexes may serve as type II ICD inducers due to their excellent ER localisation and efficient ROS generation. In contrast, the localisation of the complexes in normal MRC9 cells did not show any distinctive staining, and the emission intensity was significantly lower (Fig. S20). The cellular uptake of the iridium(III) complexes in cancer A549 and HeLa cells and normal MRC9 cells is listed in Table S15. The cellular uptake efficiency of all the complexes is as follows: **2** > **3** > **1** > **4** in both cancer cell lines. All the complexes showed much higher uptake efficiency in cancer cells ([Ir] = 0.44–6.10 fmol) than in normal cells ([Ir] = 0.07–1.01 fmol), which in conjunction with their localisation may account for their low photocytotoxicity towards normal cells (Table 1). Complex **2** displayed almost >2-fold greater uptake than all the other complexes across both cancer cell lines and could play an important role in its larger photocytotoxic activity. Importantly, all the iridium(III) complexes are potent photosensitisers with exquisite selectivity towards cancer cells. Complex **2** was used as a model to further study the specific ROS generated intracellularly (Fig. 3b) and the cellular uptake mechanism (Fig. 3c) owing to its high cellular uptake efficiency and large PI values. The photoinduced ROS generated in HeLa cells was characterised by treatment with ROS inhibitors and the ROS indicator CM-H_2DCFDA. Strong fluorescence of the probe was observed upon irradiation of complex **2** alone, indicating the generation of ROS. Pretreatment of HeLa cells with Tiron and NaN_3 ($O_2^{-\bullet}$ and $^1O_2$ scavengers, respectively) led to a sharp decrease in the fluorescence intensity of the ROS indicator. Interestingly, this result indicates that the mesoionic N^S iridium(III) complexes may activate both type I and type II PDT pathways. The cellular uptake mechanism was determined by blocking various pathways *via* preincubation with different inhibitors in HeLa cells. Upon pretreatment with endocytic or metabolic inhibitors, the internalisation of complex **2** was reduced, suggestive of a primarily energy-dependent endocytosis pathway. This result was further confirmed by preincubation of

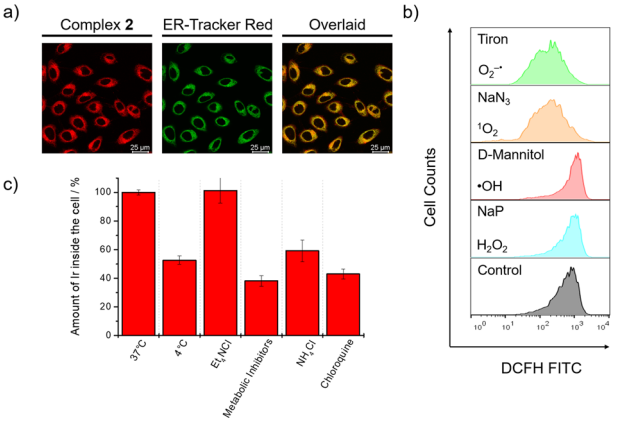

Fig. 3 (a) Laser-scanning confocal microscopy of HeLa cells treated with complex **2** (10 μM, 24 h, λ_{ex} = 405 nm; λ_{em} = 540–570 nm) and further incubated with ER-Tracker Red (1 μM, 30 min, λ_{ex} = 587 nm; λ_{em} = 610–630 nm) (PCC = 0.90). (b) Characterisation of specific ROS produced in HeLa cells incubated with complex **2** (500 nM, 24 h) upon irradiation (450 nm, 15.5 mW cm^{-2}, 15 min). Control: no ROS inhibitors. (c) Cellular uptake mechanism study of complex **2** (10 μM, 1 h) upon pretreatment with different inhibitors/under varied conditions in HeLa cells for 1 h. Control: 37 °C, low temperature: 4 °C, cation transporter inhibition: Et_4NCl (1 mM), metabolic inhibition: 2-deoxy-D-glucose (50 mM) and oligomycin (5 mM), and endocytic inhibition: NH_4Cl (50 mM) or chloroquine (100 μM).

Table 1 (Photo)cytotoxicity (IC_{50}, μM) of p-Httqt and iridium(III) complexes **1–4** towards cancer and normal cells in the dark and upon irradiation at 450 nm (15.5 mW cm^{-2}, 15 min). PI is the ratio of $IC_{50,dark}/IC_{50,light}$

	A549			HeLa			MRC9		
Compound	$IC_{50,dark}$	$IC_{50,light}$	PI	$IC_{50,dark}$	$IC_{50,light}$	PI	$IC_{50,dark}$	$IC_{50,light}$	PI
p-Httqt	>100	>100	–[a]	>100	>100	–[a]	>100	>100	–[a]
1	>50	0.027 ± 0.003	>1852	>50	0.015 ± 0.002	>3333	>50	>50	–[a]
2	>50	0.0019 ± 0.0001	>26 316	>50	0.0015 ± 0.0003	>33 333	>50	>50	–[a]
3	>50	0.014 ± 0.001	>3571	>50	0.006 ± 0.001	>8333	>50	>50	–[a]
4	>25	0.069 ± 0.02	>362	>25	0.005 ± 0.001	>5000	>25	>25	–[a]

[a] Could not be determined with accuracy.

HeLa cells at 4 °C, which also reduced the uptake efficiency of complex **2**.

Cell death mechanism

Cell death mechanisms are often characterised by morphological changes that occur during cell death and can aid or inhibit anti-tumour responses. Complex **2** was used as a model to assess the photoinduced cell death pathway by flow cytometric analysis of HeLa cells stained with Annexin V and propidium iodide. As illustrated in Fig. 4a, HeLa cells underwent apoptotic cell death in a dose-dependent manner when treated with complex **2** and light irradiation. Notably, this effect was observed at nanomolar concentrations of complex **2**, with apoptotic cells significantly increasing up to 56.2% at [Ir] = 4.5 nM. In the absence of light, complex **2** showed a negligible cell mortality rate (<3.4%), further highlighting the potent photocytotoxic activity and low dark cytotoxicity of the complex.

Apoptotic cell death is characterised by activation of caspases, changes in cell morphology and loss of mitochondrial membrane potential (MMP).[64–66] Caspases 3 and 7 are a family of inactive proteases that initiate a cascade of downstream signals at the onset of apoptosis. CellEvent™ Caspase-3/7 Red contains a peptide sequence (DEVD) specific to caspase 3/7 conjugated to a fluorogenic nucleus-specific dye and was used to monitor caspase 3/7 activation (Fig. 4b). Untreated and complex **2**-only treated HeLa cells showed no fluorescence, indicating that apoptosis was absent. However, treatment of HeLa cells with complex **2** and light irradiation led to strong fluorescence in the nuclei, demonstrating that caspase 3/7 was activated and the cells underwent apoptotic cell death. The nuclear morphology of HeLa cells upon treatment with complex **2**, with or without light irradiation, was assessed using the nuclei-specific dye Hoechst 33342 (Fig. 4c). Under dark conditions, treatment of HeLa cells with complex **2** showed a similar nuclear morphology to that of untreated HeLa cells. In contrast, the combined treatment of complex **2** and light irradiation induced nuclear condensation and fragmentation, a common hallmark of apoptosis.

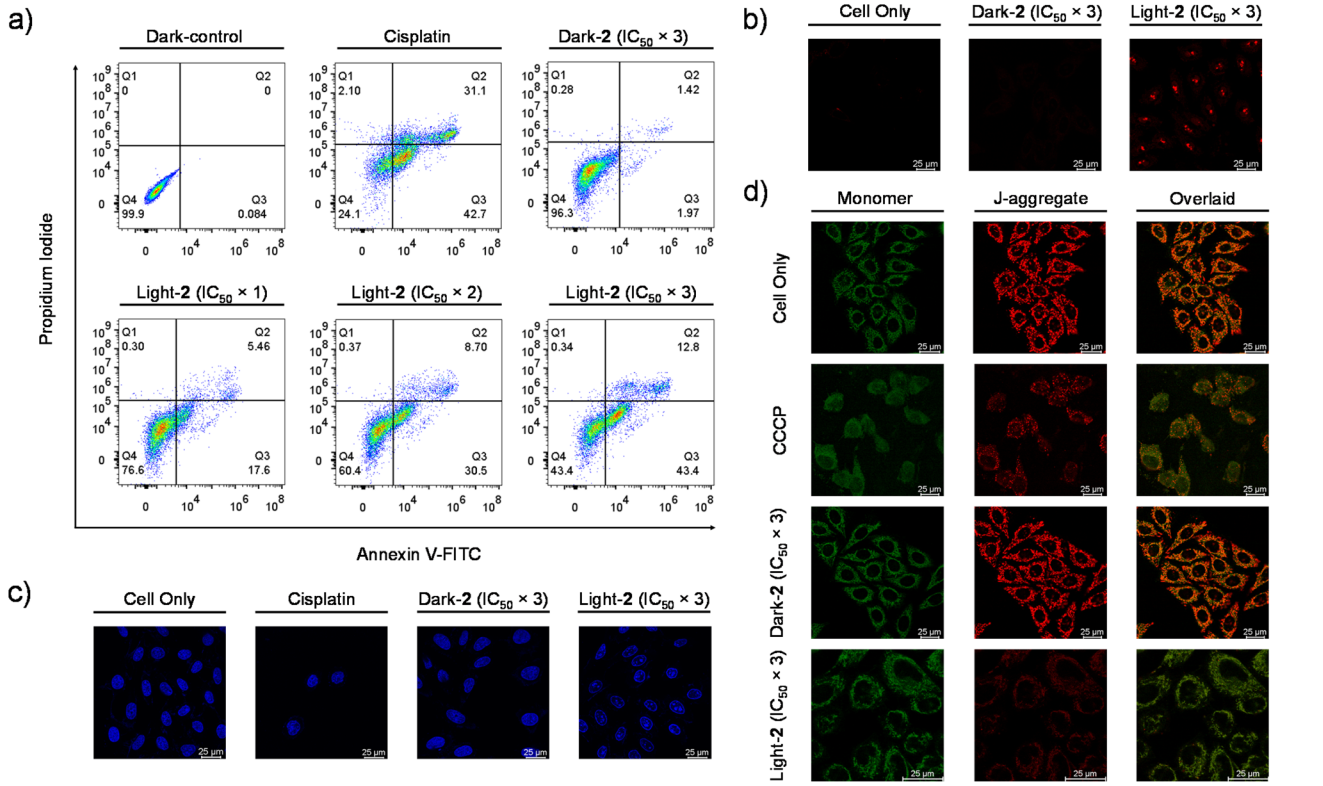

Fig. 4 (a) Dot plots of Annexin V-FITC/propidium iodide assay on HeLa cells treated with complex **2** (1.5, 3.0 and 4.5 nM) in the dark and upon light irradiation. The percentage of cell populations in the respective quadrants is shown as follows: upper left (Q1): necrotic cells, upper right (Q2): late apoptotic cells, bottom right (Q3): early apoptotic cells, and bottom left (Q4): live cells. For the dark control, the HeLa cells were left untreated. In the positive control, HeLa cells were treated with cisplatin (20 μM) for 24 h. (b) Caspase 3/7 activity of HeLa cells with no treatment or treatment with complex **2** (4.5 nM, 24 h) followed by incubation in the dark for 24 h, or treatment with complex **2** (4.5 nM, 24 h), followed by light irradiation, and further incubation for 24 h. All the samples were stained with CellEvent™ Caspase-3/7 Red (20 μL, 1 : 100, 1 h, λ_{ex} = 590 nm; λ_{em} = 610–630 nm). (c) Nuclear morphology of HeLa cells with no treatment, treatment with cisplatin (20 μM, 24 h), treatment with complex **2** (4.5 nM, 24 h) followed by incubation in the dark for 24 h, and treatment with complex **2** (4.5 nM, 24 h), followed by light irradiation, and further incubation for 24 h. All the samples were stained with Hoechst 33342 (0.5 μg mL^{-1}, 15 min, λ_{ex} = 405 nm; λ_{em} = 410–430 nm). (d) Mitochondrial membrane potential of HeLa cells with no treatment, treatment with CCCP (50 μM, 15 min) only, or treatment with complex **2** (4.5 nM, 24 h) followed by incubation in the dark for 24 h, or treatment with complex **2** (4.5 nM, 24 h), followed by light irradiation, and further incubation for 24 h. All the samples were stained with JC-1 (2 μg mL^{-1}, 20 min, λ_{ex} = 488 nm; $\lambda_{em,monomer}$ = 510–530 nm; $\lambda_{em,j\text{-}aggregate}$ = 590–610 nm). In all the experiments, light irradiation = 450 nm, 15.5 mW cm^{-2}, 15 min.

In apoptotic cell death, the loss of MMP triggers the release of signalling proteins that activate apoptotic markers (caspases, cytochrome *c* and apoptosis-inducing factors). The MMP of HeLa cells in response to complex **2** was monitored with JC-1, a mitochondria-specific dye exhibiting green (monomeric) and red (J-aggregate) emission at low and high MMP, respectively (Fig. 4d). HeLa cells that were left untreated or incubated with complex **2** only showed similar green and red emission intensities, whereas treatment with carbonyl cyanide *m*-chlorophenyl hydrazone (CCCP, an MMP disruptor) reduced the intensity of the red channel. Similarly, the treatment of HeLa cells with complex **2** and light irradiation significantly disrupted the emission intensity of the J-aggregates, illustrating that the complex can induce loss of MMP upon excitation. Altogether, the nuclear condensation and fragmentation, caspase 3/7 activation and loss of MMP results highlight that the cell death mechanism is based on photoinduced apoptosis.

Induction of immunogenic cell death

The excellent ER-localisation ability and efficient ROS generation of complex **2** can be utilised to develop new type II ICD inducers. Type II inducers are considered more potent since the generated ROS can directly induce ER stress, a central hub necessary for activating damage-associated molecular patterns (DAMPs) and the ICD response. After photoinduced apoptosis by complex **2**, ICD hallmarks like ER stress, exposure of calreticulin on the membrane surface, and extracellular release of high mobility group box-1 (HMGB1) and ATP were evaluated in HeLa cells. One function of the ER is calcium homeostasis, and impairment of this role by ROS can induce ER stress that ultimately triggers an inflammatory response.[67–70] The calcium release from the ER into the cytoplasm after irradiation was determined using Fluo-4 AM, a fluorogenic dye responsive to the spatial dynamics of calcium signalling (Fig. 5a). Incubation of complex **2** with light irradiation resulted in a significant elevation of cytoplasmic calcium concentration compared to the dark condition, suggesting that the ROS generated by complex **2** during photoirradiation can induce ER stress.

Calreticulin, a major DAMP marker, resides in the ER but translocates during ER stress and early apoptotic phases to the surface of the plasma membrane as an "eat me signal" for recognition by dendritic cells, leading to anti-tumoural

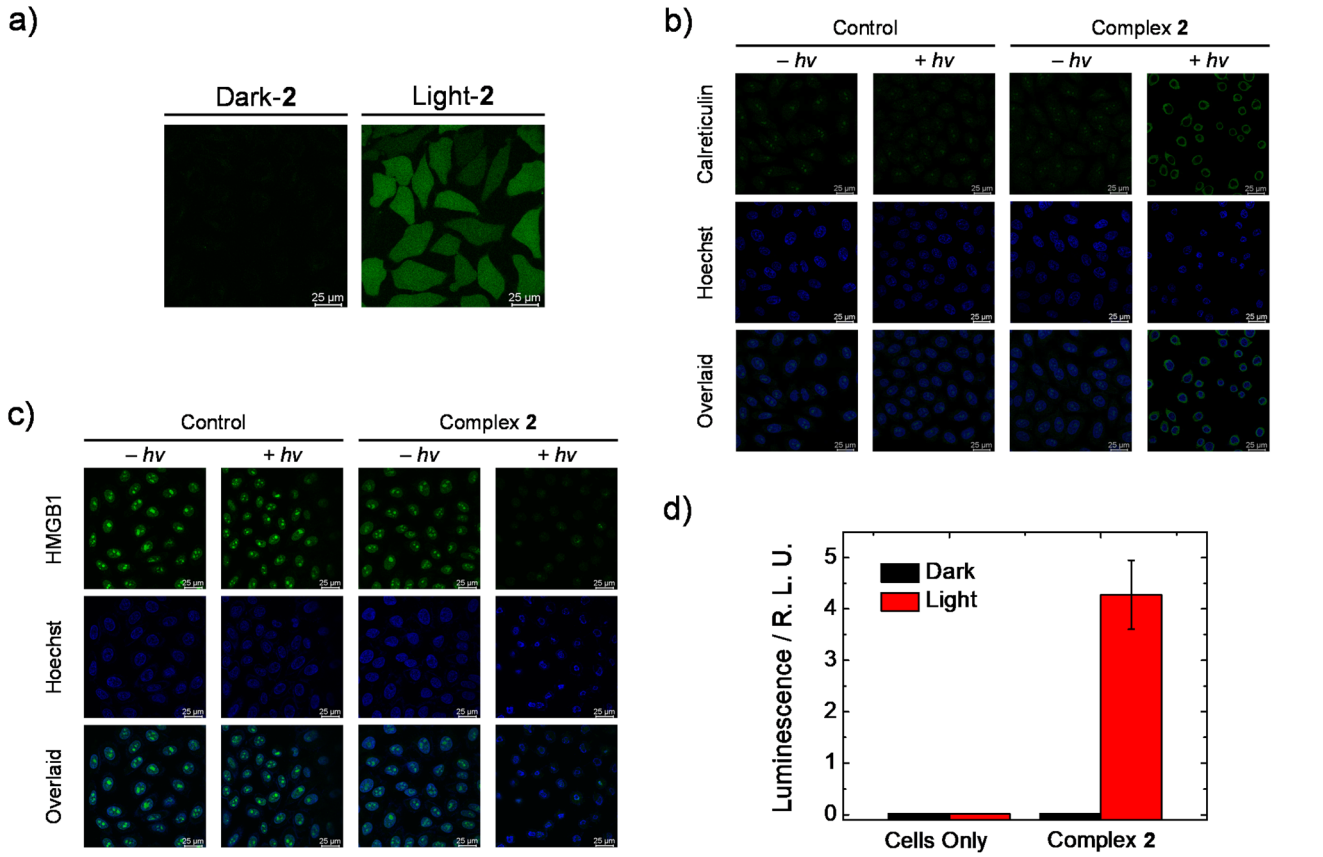

Fig. 5 (a) Intracellular calcium content of HeLa cells treated with complex **2** (1 μM, 24 h) without or with light irradiation, and further incubated with Fluo-4 AM (1 μM, 30 min, λ_{ex} = 488 nm, λ_{em} = 510–530 nm). (b) and (c) LSCM images of calreticulin or HMGB1 of HeLa cells with no treatment or treated with complex **2** (1 μM, 24 h), without or with light irradiation. All the samples were incubated with the anti-CALR polyclonal antibody (1 : 200) or anti-HMGB1 polyclonal antibody (1 : 200) overnight, Alexa Fluor 488-labeled goat anti-rabbit IgG (H + L) (1 : 500, λ_{ex} = 488 nm, λ_{em} = 510–530 nm) for 1 h, and Hoechst 33342 (0.5 μg mL^{-1}, 15 min, λ_{ex} = 405 nm, λ_{em} = 410–430 nm) for 15 min with PBS wash (1 mL × 3) before each subsequent treatment. (d) Extracellular ATP levels of HeLa cells treated without or with complex **2** (1 μM, 24 h) in the dark (black) or with light irradiation (red). In all the experiments, light irradiation = 450 nm, 15.5 mW cm^{-2}, 15 min.

immunity responses.[67,71] Immunofluorescence imaging showed that no surface expression of calreticulin could be detected in untreated HeLa cells under dark or light conditions, and a similar result was observed for HeLa cells only treated with complex **2** in the dark (Fig. 5b). Upon incubation with complex **2** and subsequent irradiation, green immunofluorescence was detected, revealing that surface calreticulin expression could only be induced by the phototherapeutic activity of complex **2**.

Cancer cells undergoing ICD release HMGB1 from the nucleus to the extracellular space due to the permeabilisation of the nuclear lamina and plasma membrane.[72–74] These extracellular HMGB1 molecules act as DAMPs to regulate inflammation and immune response. As shown in Fig. 5c, strong immunofluorescence staining in the nucleus was detected in untreated HeLa cells with or without irradiation as well as in HeLa cells treated with complex **2** in the dark. These results illustrate that complex **2** alone cannot translocate HMGB1 to the extracellular space. However, combining complex **2** and light irradiation reduced the emission intensity in the nucleus significantly, indicating that the photoinduced apoptotic effect of complex **2** can enable the release of HMGB1 to the extracellular space.

The secretion of ATP into the extracellular space was determined using a bioluminescence assay. During ICD, the extracellular release of ATP functions as a "find me" signal to enhance tumour recognition by immune cells.[68,74,75] Notably, only HeLa cells treated with complex **2** and light irradiation induced the extracellular release of ATP. After photoirradiation, a sharp increase in luminescence was observed (Fig. 5d), corresponding to the extracellular release of ATP. Summing up, from the ER stress, exposure of calreticulin on the membrane surface and extracellular release of HMGB1 and ATP experiments, complex **2** can be identified as a new PDT-based type II ICD inducer.

Conclusion

We have explored an unusual and rare class of mesoionic N^S biscyclometallated iridium(III) complexes and their surprising potency as photosensitisers and photoactivated type II ICD inducers. Using X-ray crystallography and DFT studies, we demonstrate the retention and elucidation of the "mesoionic" character of the complexes after coordination with the p-Httqt ligand. All the complexes are remarkably effective photosensitisers with no cytotoxicity in the dark up to micromolar concentrations ($IC_{50,dark}$ > 25 μM in cancer A549 and HeLa cells and normal MRC9 cells), and exhibited extremely high photocytotoxic activity against cancer cells at nanomolar concentrations ($IC_{50,light}$ = 0.0019–0.069 and 0.0015–0.006 μM in A549 and HeLa cells, respectively) with some of the largest PI values (PI = 362–26 316 and 3333–33 333 in A549 and HeLa cells, respectively) reported to date for biscyclometallated iridium(III) complexes, along with selective photocytotoxicity towards cancer cells. Furthermore, the good ER localisation and $^1O_2$ generation capabilities of all the iridium(III) complexes enable their use as PDT-activated type II ICD inducers. Complex **2** displayed the highest photocytotoxic activity and was used as a model to illustrate the uptake pathway, cell death mechanism and the activation of DAMPs during ICD.

Author contributions

J. S.: conceptualisation, data curation, formal analysis, investigation, writing – original draft, writing – reviewing & editing; P. K.-K. L.: conceptualisation, data curation, formal analysis; L. H.: data curation, formal analysis, writing – reviewing & editing; L. C.-C. L.: data curation, formal analysis; M. Y.: data curation; L. C.: data curation, formal analysis; Y. P.: data curation, formal analysis; M. W.-L. C.: data curation; K. S.-M. Y.: data curation, formal analysis; K.-C. L.: supervision, writing – review & editing; B. Z. T.: funding acquisition, project administration, supervision, writing – review & editing; K. K.-W. L.: conceptualisation, funding acquisition, project administration, resources, supervision, writing – original draft, writing – review & editing.

Conflicts of interest

There are no conflicts to declare.

Data availability

CCDC 2296948, 2296949 and 2296950 contain the supplementary crystallographic data for this paper.[76a–c]

The data that support the findings of this study are available in the SI of this article. Supplementary information: instrumentation, methods, synthetic details, characterisation, analytical and photophysical data, DFT calculations and microscopy experiments. See DOI: **https://doi.org/10.1039/d5sc04772b**.

Acknowledgements

We thank the Hong Kong Research Grants Council (Project No. CityU 11301121, CityU 11317022, CityU 11309423 and C7075-21 GF) and the Hong Kong Research Grants Council and National Natural Science Foundation of China Joint Scheme (Project No. N_CityU104/21) for financial support. We also acknowledge the funding support from the "Laboratory for Synthetic Chemistry and Chemical Biology" under the Health@InnoHK Programme launched by the Innovation and Technology Commission, The Government of Hong Kong SAR, P. R. China.

References

1 W. Baker and W. D. Ollis, *Q. Rev. Chem. Soc.*, 1957, **11**, 15.
2 P. A. Champagne and K. N. Houk, *J. Org. Chem.*, 2017, **82**, 10980.
3 S. Wiechmann, T. Freese, M. H. H. Drafz, E. G. Hübner, J. C. Namyslo, M. Nieger and A. Schmidt, *Chem. Commun.*, 2014, **50**, 11822.
4 X. Bantreil, N. Pétry and F. Lamaty, *Dalton Trans.*, 2019, **48**, 15753.
5 J. R. Ames, K. T. Potts, M. D. Ryan and P. Kovacic, *Life Sci.*, 1986, **39**, 1085.

6 D. Liu, J. Zhang, L. Zhao, W. He, Z. Liu, X. Gan and B. Song, *J. Agric. Food Chem.*, 2019, **67**, 11860.
7 K. Rehse, K.-J. Schleifer, A. Martens and M. Kämpfe, *Arch. Pharm.*, 1994, **327**, 393.
8 A. W. Brown, T. Holmes, M. Fischer, G. M. Tozer, J. P. A. Harrity and C. Kanthou, *ChemMedChem*, 2018, **13**, 2618.
9 A. Senff-Ribeiro, A. Echevarria, E. F. Silva, C. R. C. Franco, S. S. Veiga and M. B. M. Oliveira, *Br. J. Cancer*, 2004, **91**, 297.
10 J. C. Cardoso, S. M. S. C. Cadena, A. Zampronio, A. M. S. Arruda, E. G. S. Carnieri, A. Echevarria, J. Constantin, A. Bracht and M. B. M. Oliveira, *Drug Dev. Res.*, 2004, **61**, 207.
11 S. M. Kovalenko, O. G. Drushlyak and I. O. Mariutsa, *J. Sulfur Chem.*, 2019, **41**, 388.
12 X. Zhao, J. Liu, J. Fan, H. Chao and X. Peng, *Chem. Soc. Rev.*, 2021, **50**, 4185.
13 A. Zamora, G. Vigueras, V. Rodríguez, M. D. Santana and J. Ruiz, *Coord. Chem. Rev.*, 2018, **360**, 34.
14 B. Kar, U. Das, N. Roy and P. Paira, *Coord. Chem. Rev.*, 2023, **474**, 214860.
15 Y. Wu, S. Li, Y. Chen, W. He and Z. Guo, *Chem. Sci.*, 2022, **13**, 5085.
16 L. Huang, L. C.-C. Lee, J. Shum, G.-X. Xu and K. K.-W. Lo, *Chem. Commun.*, 2024, **60**, 6186.
17 L. C.-C. Lee and K. K.-W. Lo, *Chem. Rev.*, 2024, **124**, 8825.
18 E. C.-L. Mak, Z. Chen, L. C.-C. Lee, P. K.-K. Leung, A. M.-H. Yip, J. Shum, S.-M. Yiu, V. W.-W. Yam and K. K.-W. Lo, *J. Am. Chem. Soc.*, 2024, **146**, 25589.
19 L. C.-C. Lee and K. K.-W. Lo, *Small Methods*, 2024, **8**, 2400563.
20 S. Sen, M. Won, M. S. Levine, Y. Noh, A. C. Sedgwick, J. S. Kim, J. L. Sessler and J. F. Arambula, *Chem. Soc. Rev.*, 2022, **51**, 1212.
21 K. Xiong, F. Wei, Y. Chen, L. Ji and H. Chao, *Small Methods*, 2022, **7**, 2201403.
22 Z.-Y. Li, Q.-H. Shen, Z.-W. Mao and C.-P. Tan, *Chem.–Asian J.*, 2022, **17**, e20220270.
23 L. Zhang, N. Montesdeoca, J. Karges and H. Xiao, *Angew. Chem., Int. Ed.*, 2023, **62**, e202300662.
24 A. P. King and J. J. Wilson, *Chem. Soc. Rev.*, 2020, **49**, 8113.
25 J.-Y. Zhou, Q.-H. Shen, X.-J. Hong, W.-Y. Zhang, Q. Su, W.-G. Li, B. Cheng, C.-P. Tan and T. Wu, *Chem. Eng. J.*, 2023, **474**, 145516.
26 L. Wang, R. Guan, L. Xie, X. Liao, K. Xiong, T. W. Rees, Y. Chen, L. Ji and H. Chao, *Angew. Chem., Int. Ed.*, 2020, **133**, 4707.
27 W.-S. Sie, J.-Y. Jian, T.-C. Su, G.-H. Lee, H. M. Lee and K.-B. Shiu, *J. Organomet. Chem.*, 2008, **693**, 1510.
28 Y. You, S. Cho and W. Nam, *Inorg. Chem.*, 2014, **53**, 1804.
29 J. Ruiz, C. Vicente, C. de Haro and D. Bautista, *Inorg. Chem.*, 2013, **52**, 974.
30 A. M. Simas, J. Miller and P. F. de Athayade Filho, *Can. J. Chem.*, 1998, **76**, 869.
31 Y. I. Nein and Y. Y. Morzherin, *Russ. Chem. Bull.*, 2012, **61**, 1111.
32 W. P. Oziminski and C. A. Ramsden, *Tetrahedron*, 2015, **71**, 7191.
33 D. Sambade, C. Collins and G. Parkin, *J. Mol. Struct.*, 2021, **1231**, 129682.
34 N. Takeda, N. Tokitoh and R. Okazaki, *Chem.–Eur. J.*, 1997, **3**, 62.
35 A. P. Cox, S. D. Hubbard and H. Kato, *J. Mol. Spectrosc.*, 1982, **93**, 196.
36 T. Y. Fu, J. R. Scheffer and J. Trotter, *Acta Crystallogr. C Struct. Chem.*, 1997, **53**, 1257.
37 K. Porte, M. Riomet, C. Figliola, D. Audisio and F. Taran, *Chem. Rev.*, 2021, **121**, 6718.
38 K. Y. Zhang, H.-W. Liu, M.-C. Tang, A. W.-T. Choi, N. Zhu, X.-G. Wei, K.-C. Lau and K. K.-W. Lo, *Inorg. Chem.*, 2015, **54**, 6582.
39 K. K.-W. Lo, K. Y. Zhang, C.-K. Chung and K.-Y. Kwok, *Chem.–Eur. J.*, 2007, **13**, 7110.
40 K. K.-W. Lo, J. S.-W. Chan, L.-H. Hui and C.-K. Chung, *Organometallics*, 2004, **23**, 3108.
41 K. K.-W. Lo, C.-K. Li and J. S.-Y. Lau, *Organometallics*, 2005, **24**, 4594.
42 L. C.-C. Lee, A. W.-Y. Tsang, H.-W. Liu and K. K.-W. Lo, *Inorg. Chem.*, 2020, **59**, 14796.
43 C. K. Prier, D. A. Rankic and D. W. C. Macmillan, *Chem. Rev.*, 2013, **113**, 5322.
44 Y. Dong, J. W.-Y. Lam, A. Qin, J. Sun, J. Liu, Z. Li, J. Sun, H. H.-Y. Sung, I. D. Williams, H. S. Kwok and B. Z. Tang, *Chem. Commun.*, 2007, 3255.
45 V. Sathish, A. Ramdass, P. Thanasekaran, K.-L. Lu and S. J. Rajagopal, *Photochem. Photobiol. C*, 2015, **23**, 25.
46 A. Chiarugi, C. Dölle, R. Felici and M. Ziegler, *Nat. Rev. Chem.*, 2012, **12**, 741.
47 L. Wei, R. Kushwaha, A. Dao, Z. Fan, S. Banerjee and H. Huang, *Chem. Commun.*, 2023, **59**, 3083.
48 Y. Yang, Y. Gao, J. Zhao and S. Gou, *Inorg. Chem. Front.*, 2024, **11**, 436.
49 J. Kasparkova, A. Hernández-García, H. Kostrhunova, M. Goicuría, V. Novohradsky, D. Bautista, L. Markova, M. D. Santana, V. Brabec and J. Ruiz, *J. Med. Chem.*, 2024, **67**, 691.
50 Z. Fan, J. Xie, R. Kushwaha, S. Liang, W. Li, A. A. Mandal, L. Wei, S. Banerjee and H. Huang, *Chem.–Asian J.*, 2023, **18**, e202300047.
51 Z. Fan, Y. Rong, T. Sadhukhan, S. Liang, W. Li, Z. Yuan, Z. Zhu, S. Guo, S. Ji, J. Wang, R. Kushwaha, S. Banerjee, K. Raghavachari and H. Huang, *Angew. Chem., Int. Ed.*, 2022, **61**, e202202098.
52 D. T. Sawyer and J. L. Jr. Roberts, *J. Electroanal. Chem.*, 1966, **12**, 90.
53 C. Huang, C. Liang, T. Sadhukhan, S. Banerjee, Z. Fan, T. Li, Z. Zhu, P. Zhang, K. Raghavachari and H. Huang, *Angew. Chem., Int. Ed.*, 2021, **60**, 9474.
54 Z. Fan, J. Xie, T. Sadhukhan, C. Liang, C. Huang, W. Li, T. Li, P. Zhang, S. Banerjee, K. Raghavachari and H. Huang, *Chem.–Eur. J.*, 2022, **28**, e202103346.
55 R. F. Anderson, *Biochim. Biophys. Acta – Bioenerg.*, 1980, **590**, 277.

56 H. Huang, S. Banerjee, K. Qiu, P. Zhang, O. Blacque, T. Malcomson, M. J. Paterson, G. J. Clarkson, M. Staniforth, V. G. Stavros, G. Gasser, H. Chao and P. J. Sadler, *Nat. Chem.*, 2019, **11**, 1041.
57 L. He, C.-P. Tan, R.-R. Ye, M.-H. Chen, J.-J. Cao, L.-N. Ji and Z.-W. Mao, *Chem. Sci.*, 2015, **6**, 5409.
58 M. Ouyang, L. Zeng, K. Qiu, Y. Chen, L. Ji and H. Chao, *Eur. J. Inorg. Chem.*, 2017, **2017**, 1764.
59 Y. You, E. J. Cho, H. Kwon, J. Hwang and S. E. Lee, *Chem. Commun.*, 2016, **52**, 780.
60 P. Zhang, H. Huang, S. Banerjee, G. J. Clarkson, C. Ge, C. Imberti and P. J. Sadler, *Angew. Chem., Int. Ed.*, 2018, **58**, 2350.
61 L. He, M.-F. Zhang, Z.-Y. Pan, K.-N. Wang, Z.-J. Zhao, Y. Li and Z.-W. Mao, *Chem. Commun.*, 2019, **55**, 10472.
62 B. Yuan, J. Liu, R. Guan, C. Jin, L. Ji and H. Chao, *Dalton Trans.*, 2019, **48**, 6408.
63 W.-W. Qin, Z.-Y. Pan, D.-H. Cai, Y. Li and L. He, *Dalton Trans.*, 2020, **49**, 3562.
64 J. F. R. Kerr, A. H. Wyllie and A. R. Currie, *Br. J. Cancer*, 1972, **26**, 239.
65 R. A. Schwartzman and J. A. Cidlowski, *Endocr. Rev.*, 1993, **14**, 133.
66 S. J. Riedl and Y. Shi, *Nat. Rev. Mol. Cell Biol.*, 2004, **5**, 897.
67 Y. Xi, L. Chen, J. Tang, B. Yu, W. Shen and X. Niu, *Immunol. Rev.*, 2023, **321**, 94.
68 D. V. Krysko, A. D. Garg, A. Kaczmarek, O. Krysko, P. Agostinis and P. Vandenabeele, *Nat. Rev. Cancer*, 2012, **12**, 860.
69 D. Xie, Q. Wang and G. Wu, *Front. Immunol.*, 2022, **13**, 1017400.
70 J. Fucikova, O. Kepp, L. Kasikova, G. Petroni, T. Yamazaki, P. Liu, L. Zhao, R. Spisek, G. Kroemer and L. Galluzzi, *Cell Death Dis.*, 2020, **11**, 1013.
71 T. Panaretakis, O. Kepp, U. Brockmeier, A. Tesniere, A.-C. Bjorklund, D. C. Chapman, M. Durchschlag, N. Joza, G. Pierron, P. van Endert, J. Yuan, L. Zitvogel, F. Madeo, D. B. Williams and G. Kroemer, *EMBO J.*, 2009, **28**, 578.
72 R. Chen, R. Kang and D. Tang, *Exp. Mol. Med.*, 2022, **54**, 91.
73 M. S. Kwak, H. S. Kim, B. Lee, Y. H. Kim, M. Son and J.-S. Shin, *Front. Immunol.*, 2020, **11**, 1189.
74 O. Krysko, T. L. Aaes, C. Bachert, P. Vandenabeele and D. V. Krysko, *Cell Death Dis.*, 2013, **4**, e631.
75 I. Martins, Y. Wang, M. Michaud, Y. Ma, A. Q. Sukkurwala, S. Shen, O. Kepp, D. Métivier, L. Galluzzi, J.-L. Perfettini, L. Zitvogel and G. Kroemer, *Cell Death Differ.*, 2014, **4**, 79.
76 (*a*) J. Shum, P. K.-K. Leung, L. Huang, L. C.-C. Lee, M. Yarshova, L. Cheng, Y. Pan, M. W.-L. Chiang, K. S.-M. Yiu, K.-C. Lau, B. Z. Tang and K. K.-W. Lo, CCDC 2296948, Experimental Crystal Structure Determination, 2025, DOI: **10.5517/ccdc.csd.cc2h353x**; (*b*) J. Shum, P. K.-K. Leung, L. Huang, L. C.-C. Lee, M. Yarshova, L. Cheng, Y. Pan, M. W.-L. Chiang, K. S.-M. Yiu, K.-C. Lau, B. Z. Tang and K. K.-W. Lo, CCDC 2296949, Experimental Crystal Structure Determination, 2025, DOI: **10.5517/ccdc.csd.cc2h354y**; (*c*) J. Shum, P. K.-K. Leung, L. Huang, L. C.-C. Lee, M. Yarshova, L. Cheng, Y. Pan, M. W.-L. Chiang, K. S.-M. Yiu, K.-C. Lau, B. Z. Tang and K. K.-W. Lo, CCDC 2296950, Experimental Crystal Structure Determination, 2025, DOI: **10.5517/ccdc.csd.cc2h355z**.